



# Effect of Oxidizer on PANI for Producing BaTiO<sub>3</sub>@PANI Perovskite Composites and Their Electrical and Electrochemical Properties

Khaled F. Qasim<sup>1</sup> · Mahmoud A. Mousa<sup>2</sup>

Received: 11 January 2022 / Accepted: 31 March 2022  
© The Author(s) 2022

## Abstract

Polyaniline (PANI) has received significant attention in basic and applied studies because it has electrical and electrochemical properties comparable to conventional semiconductors and metals. PANI's electrical and electrochemical properties can be controlled through its preparation methods. Accordingly, in the present work, two different samples of PANI were prepared by the polymerization of aniline monomer via in situ polymerization method using two different oxidizers of dichromate (PANI (1)) and persulphate (PANI (2)). The products were blended with BaTiO<sub>3</sub> (BTO) to form BTO@PANI composites. The composites were characterized by scanning electron microscopy (SEM), Fourier transforms infrared spectroscopy (FTIR), X-ray powder diffraction (XRD), and X-ray photoelectron spectroscopy (XPS). SEM illustrated the covering of PANI layers on the BTO nanoparticles. The electrical and electrochemical properties of the prepared composites were studied. The BTO@PANI(2) composite sample showed a conductivity of  $1.2 \times 10^{-3}$  S/cm higher than that found for each BTO@PANI(1)  $9.1 \times 10^{-4}$  S/cm and its constituents. The supercapacity showed higher capacity values of 70 F/g, and 76 F/g for BTO@PANI(1), and BTO@PANI(2), respectively, which are higher than its constituents.

**Keywords** Core–shell structure · Inorganic perovskite · Composites · Conducting polymers · Supercapacitor · Dielectric

## 1 Introduction

Promising steps have been taken forward for so-called flexible electronics technology devices based on flexible plastic and polymeric materials [1]. Several polymers like polyethylene (PE), polypropylene (PP), polyisobutylene (PIB), polytetrafluoroethylene (PTFE), and polyvinylidene fluoride (PVF) have been used in making flexible capacitors because of their low cost, good flexibility, and lightweight [2]. However, their low dielectric constant ( $\epsilon$ ) limited their use in fabricating high-energy-density supercapacitors [3]. Therefore, massive efforts have been organized to produce high permittivity ( $k$ ) polymeric materials to manufacture high-energy-density supercapacitors. This can be done by creating composites of a polymeric matrix with several inorganic or

organic materials such as ceramic, carbon-based materials (Graphene, CNT, etc.) [4], conducting polymers like (polyaniline (PANI) [5], polypyrrole (PPy) [6], poly(3,4-ethylene dioxythiophene) (PEDOT) [7], etc.), or metal nanoparticles [8, 9].

Anno, et al. reported that the addition of high ( $k$ ) ceramic material to polymer increases the dielectric constant ( $\epsilon$ ) many tens if the ceramic volume content exceeds 50% [2]. The effective  $\epsilon$ -values of polymers are also enhanced with a small amount of conductive filler due to the percolation of the insulator–conductor [10]. However, the resultant composite shows an excellent drawback for supercapacitor applications due to the high value of dielectric loss and current leakage. So, the real challenge in the electronic section is to develop as high ( $k$ ) and low dielectric loss composites using small traces of conductive fillers as possible.

Upgrading the binary composite to ternary composite with high ( $k$ ) inorganic fillers can improve the dielectric properties more than obtained by binary composite. Nan et al. reported that the addition of spherical Ni particles to a binary composite of PVF and BTO produced a material with high  $k$  near the percolation threshold of nickel particles [11]. The addition of carbon-based materials like CNT with high

✉ Khaled F. Qasim  
khaled\_faisal92@hotmail.com;  
Khaled.Faisal@sci.suezuni.edu.eg

<sup>1</sup> Faculty of Science, Chemistry Department, Suez University, Suez, Egypt

<sup>2</sup> Faculty of Science, Chemistry Department, Benha University, Benha, Egypt

ratios as conductive fillers for polymeric-inorganic composite materials produced composite with high ( $k$ ) and low percolation thresholds. For example, a PVDF-based composite with a high  $k$  was realized by blending with CNTs and BTO nanoparticles [4, 12].

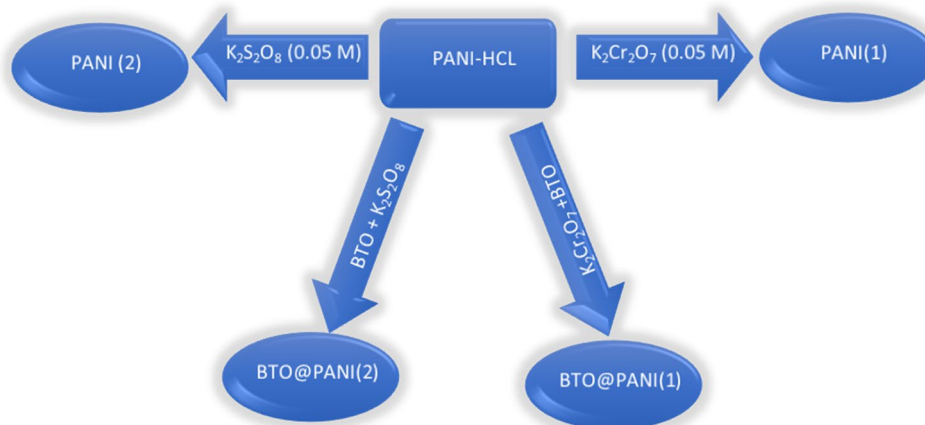
Conducting polymers (CPs) have elicited much interest among researchers because of their reasonably high conductivity, stability, affordability, and redox properties compared to other organic compounds [13, 14]. The coupling of CPs with other materials can result in attractive properties and new applications such as fabricating electrochemical

## 2.1 Preparation of BaTiO<sub>3</sub>

Ba(NO<sub>3</sub>)<sub>2</sub> and TiO<sub>2</sub> with a mass ratio of 1:1 were mixed in a dry ball mill for 24 h, followed by calcination at 800 °C for 1 h.

## 2.2 Preparation of Polyaniline

Two different polyaniline samples were synthesized using different oxidizing agents, namely K<sub>2</sub>Cr<sub>2</sub>O<sub>7</sub> and K<sub>2</sub>S<sub>2</sub>O<sub>8</sub> as presented in the next flowchart.



devices [15, 16]. Among the conducting polymers, PANI and its composites with other materials can easily be synthesized by different technique like chemical, mechanical, and electrochemical method through oxidative polymerization [17]. Polyaniline (PANI) has been implemented with other materials in their native states to form new materials with specialized applications [18] like design of various high-tech devices and technological applications such as corrosion preventing layers [19], solar cells, super capacitors [20], coatings for electromagnetic shielding, sensors, and biosensors [21–23].

In this work, we report the fabrication and the electrical properties of a novel hybrid system consisting of BaTiO<sub>3</sub> (BTO) nanoparticles, polyaniline (PANI), the applications of the prepared composites as electrodes for supercapacitor devices were studied.

## 2 Experimental

All chemicals were of reagent grades and used as received.

### 2.2.1 Preparation of Polyaniline (PANI (1))

PANI was prepared by chemical polymerization [24, 25]. 3 ml of aniline was mixed with 100 ml of 1 M of HCl to get aniline hydrochloride salt. 100 ml of 0.05 M K<sub>2</sub>Cr<sub>2</sub>O<sub>7</sub>, used as an oxidant, was titrated with aniline under stirring for 4 h in an ice bath. The powder obtained was kept in the solution for a day before filtrating and washing with distilled water and methanol. Eventually, the resultant green powder was dried at 45 °C for several hours until getting a constant weight of the sample.

### 2.2.2 Preparation of Polyaniline (PANI (2))

The same previously-mentioned procedure used in Sect. 2.2.1 was applied to prepare (PANI (2)) except using K<sub>2</sub>S<sub>2</sub>O<sub>8</sub> as an oxidant material instead of K<sub>2</sub>Cr<sub>2</sub>O<sub>7</sub>.

## 2.3 Preparation of Polymer-Based Composites

Each of the synthesized two polyaniline samples was blended with BaTiO<sub>2</sub> to form two composite samples.

### 2.3.1 Preparation of BTO@PANI (1) Composite

0.75 gm BTO was stirred in 100 ml 0.1 M aniline hydrochloride. 100 ml of 0.05 M of  $K_2Cr_2O_7$  was titrated in aniline monomer solution at 10 °C for 3 h with stirring; then, the mixture was held for one day to allow further polymerization. The product was washed with 200 ml distilled water, then filtrated and dried in an oven at 50 °C for 24 h.

### 2.3.2 Preparation of (BTO@PANI (2) Composite

It was prepared using the same previously mentioned method in Sect. 2.3.1, except using  $K_2S_2O_8$  as an oxidant material instead of  $K_2Cr_2O_7$ .

## 2.4 Characterization

XRD analyses were performed by a Philips X-ray diffractometer using Cu-K $\alpha$  with  $\lambda = 0.154$  nm. The diffractogram was recorded for  $2\theta$  angles in the range 15–80°. FT-IR spectra were recorded in the range of 4000–400  $cm^{-1}$  using an infrared spectrophotometer (Perkin- Elmer LX 18–5255). X-ray Photoelectron Spectroscopy (XPS) analyses were performed using a KRATOS XSAM-800. The thermal stability was investigated using the TGA Shimadzu model TGA-50H under  $N_2$  atmosphere at a heating rate of 10 °K/min. The morphology of the materials was analyzed by using a scanning electron microscope (SEM) (JEOL-JSM-6510 LV). Electrical properties were measured by GW Instek 8110G LCR meter, Taiwan, at a  $10^3$ – $10^7$  Hz frequency range at room temperature.

## 2.5 Electrochemical and Electric Measurements

### 2.5.1 Preparation of Working Electrodes

Electrodes were prepared by coating a paste formed from investigated materials, acetylene black and polyvinylidene fluoride with a mass ratio of 75:15:10, respectively, with ethanol as a solvent on FTO and dried at 80 °C for 2 h to vaporize the solvent.

Electrochemical behaviors of the investigated materials were studied by Galvanostatic charge–discharge (GCD) and cyclic voltammetry (CV) using a potentiostat (Digi-Ivy 2116, USA). Electrochemical impedance spectroscopy (EIS) was measured on a Metrohm autolab PGSTAT 204, Netherlands, at a constant potential of 10 mV, and frequency ranged from  $10^{-1}$  to  $10^5$  Hz. The electrochemical studies were carried out in a three-electrode cell with the prepared active material coated on FTO glass works as a working electrode, Pt sheet (2  $cm^2$ ), and saturated calomel electrode, as a counter a reference electrode, respectively. The CV was performed between – 1 and 1.2 V at a scan rate of 5 mV/s.

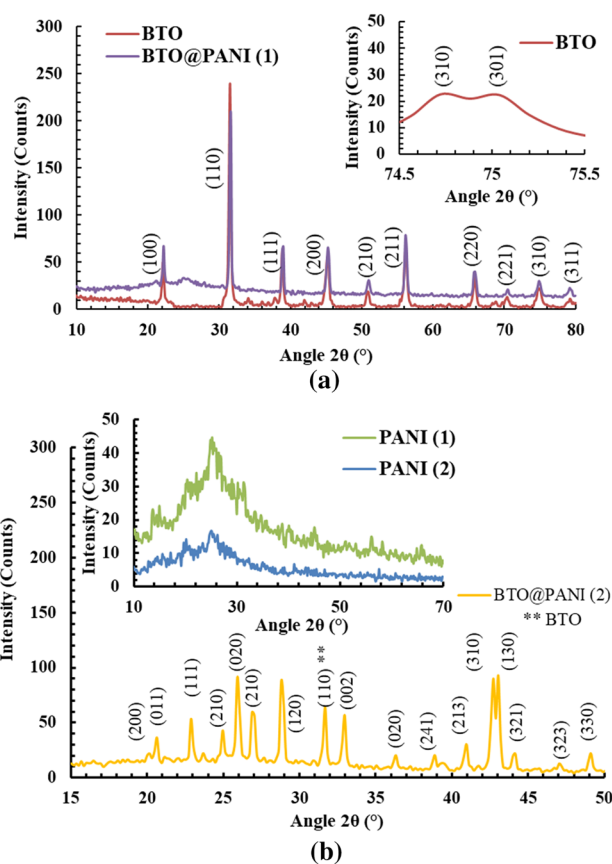


**Fig. 1** XRD of **a** BTO & BTO@PANI (1) samples, and **b** BTO@PANI (2) & PANI samples

GCD was measured at a current density of 1 A/g. All measurements were carried out in a 1 M  $LiNO_3$  aqueous electrolyte solution.

## 3 Results and Discussion

### 3.1 Chemical Characterizations

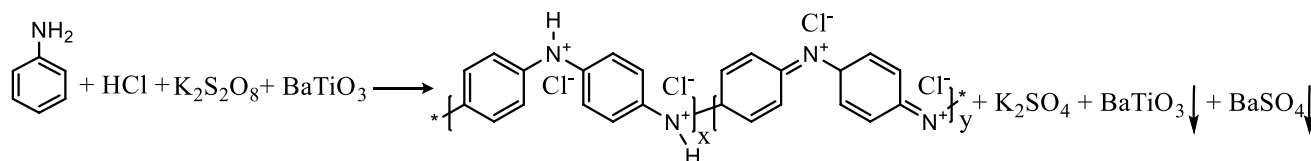
The XRD patterns of the synthesized  $BaTiO_3$  (BTO) are shown in Fig. 1a. The figure shows the characterized peaks of  $BaTiO_3$  tetragonal crystal structure with diffraction peaks at  $2\theta = 22^\circ, 31.5^\circ, 39^\circ, 45^\circ, 51^\circ, 56^\circ, 65^\circ, 70^\circ, 75^\circ,$  and  $79^\circ$  corresponding to (100), (110), (111), (200), (210), (211), (220), (221), (310), and (311), respectively, (JCPDS card 31–0174). The hump peaks observed at  $2\theta = 74.7^\circ$  and  $75.1^\circ$  refers to the planes of (301) and (310), respectively, which are present only in the tetragonal structure and not found in the hexagonal, or cubic structure [11, 26]. The XRD of the BTO@PANI (1) composite sample, present in Fig. 1a, also showed the presence of the characteristic peaks of BTO, but with low intensity and a slight shift to lower angles [27].

**Table 1** XRD data of the BTO and composite materials

Sample	Crystal size (nm)	$\epsilon$	Lattice parameter		
			A (Å)	c (Å)	V (Å <sup>3</sup> )
BTO	47.8	$2.7 \times 10^{-3}$	4.020	4.004	64.7
BTO@PANI (1)	42.5	$3.0 \times 10^{-3}$	4.010	4.007	64.4
BTO@PANI (2)	39.6	$3.3 \times 10^{-3}$	4.013	4.006	64.5

This shift is due to the chemical interaction between the PANI and BTO materials [28].

Figure 1b shows the XRD pattern of the two PANI samples beside that of the BTO@PANI(2) composite. The XRD patterns show diffraction peaks of PANI with an amorphous nature at about  $2\theta = 21^\circ$  and  $25^\circ$ , which are ascribed to the periodicity parallel and perpendicular to PANI chains, respectively [28]. The XRD patterns of BTO@PANI (2) show the characteristics peaks of BTO besides peaks characterized for the orthorhombic phase structure of BaSO<sub>4</sub>. The diffraction peaks of the orthorhombic phase are observed at  $20.3^\circ$ ,  $22.8^\circ$ ,  $23.9^\circ$ ,  $25.6^\circ$ ,  $26.8^\circ$ ,  $28.6^\circ$ ,  $31.7^\circ$ ,  $32.8^\circ$ ,  $36.1^\circ$ ,  $38.5^\circ$ ,  $39.8^\circ$ ,  $42.5^\circ$ ,  $42.8^\circ$ ,  $43.8^\circ$ , and  $44.9^\circ$  referring to (020), (111), (200), (021), (210), (121), (211), (002), (221), (022), (122), (140), (212), (041), and (330) plans, respectively, (JCPDS card no. 35–0782) [11]. The observed peaks of BaSO<sub>4</sub> can be explained based on the formation of BaSO<sub>4</sub> during the polymerization of PANI in the presence of BaCl<sub>2</sub> with persulphate initiator [29] according to the following chemical equation.

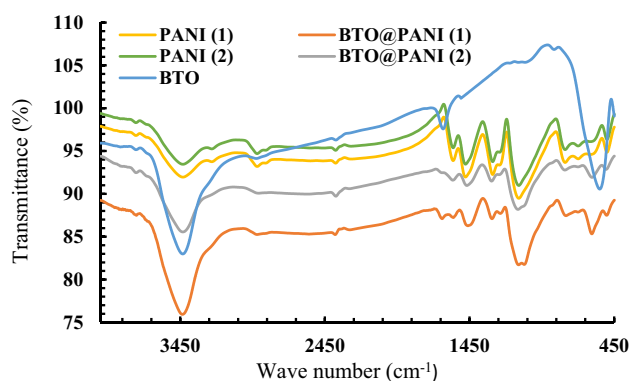


The lattice parameters and cell volume (V) of the BTO and BTO@PANI composites were evaluated by using Eqs. (1, 2), respectively, [30, 31]

$$d_{hkl} = \sqrt{\frac{a^2 + b^2}{h^2}} + \sqrt{\frac{c^2}{l^2}} \quad (1)$$

$$V = a^2 \times c \quad (2)$$

In which (hkl) are the Miller indices and both (a) and (c) is the lattice dimensions. The data obtained are listed in Table 1.

**Fig. 2** FT-IR of the investigated materials

The mean crystallite sizes and strain of the BaSO<sub>4</sub> and its composites were calculated by Debye–Scherrer's Eq. (3) [32] and strain ( $\epsilon$ ) by Eq. (4) [32].

$$D = \frac{0.9\lambda}{\beta \cos \theta} \quad (3)$$

$$\epsilon = \frac{\beta}{4 \tan \theta} \quad (4)$$

where  $\lambda$  is the X-ray wavelength used, and  $\beta$  is the half-peak width of the diffraction peak. The results obtained are

listed in Table 1, which shows that the material particles are formed in the nanoscale range, and the composites' strain is higher than that of BTO. Table 1 also shows that each particle size and the hybrid strain depend on the preparation method.

Figure 2 shows the FT-IR spectra of the investigated samples. The spectrum of BTO shows bands at  $3400 \text{ cm}^{-1}$  and  $1621 \text{ cm}^{-1}$  related to vibration of adsorbed H<sub>2</sub>O, besides a band at  $542 \text{ cm}^{-1}$  assigned to Ti–O vibration bond [2]. The FT-IR spectra of PANI and PANI@BTO show vibration bands at  $1552$  and  $1468 \text{ cm}^{-1}$  assigned to the C=C and C=N stretching bands of the quinoid and benzenoid rings, which prove the existence of an oxidized form of PANI (Pernigraniline PRG). The spectra also show bands at

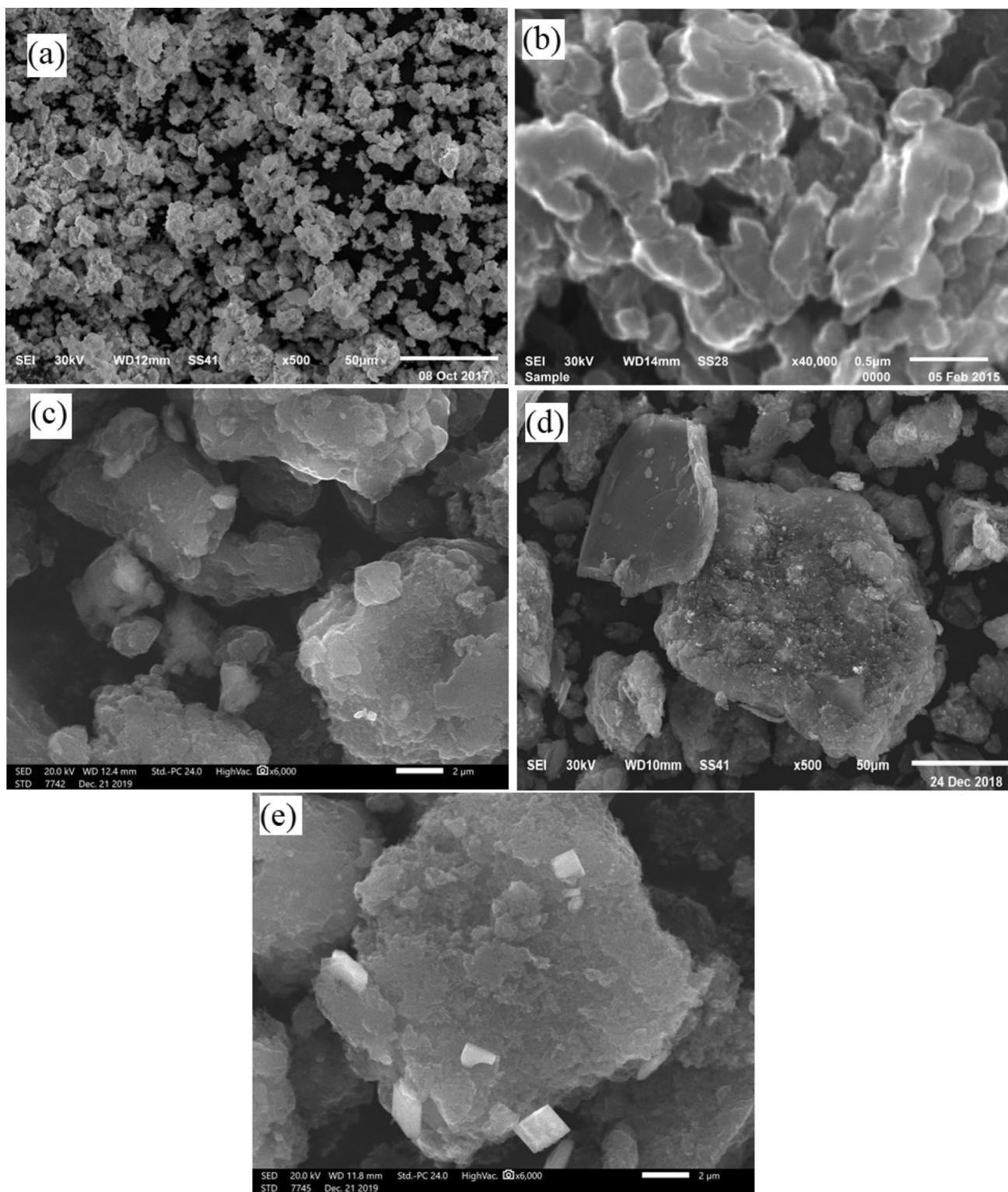


**Fig. 3** SEM of **a** BTO, **b** PANI (1), **c** PANI (2), **d** BTO@PANI (1), and **e** BTO@PANI (2)

1287 and 1235  $\text{cm}^{-1}$  attributed to N–H bending and asymmetric C–N stretching modes of the benzenoid ring, which prove the presence of a reduced form of PANI (emeraldine

salt ES) and indicated that PANI has the half-reduced form (leuco-emeraldine salt LES). The spectra of PANI and its composites also show a band near 1038  $\text{cm}^{-1}$  associated



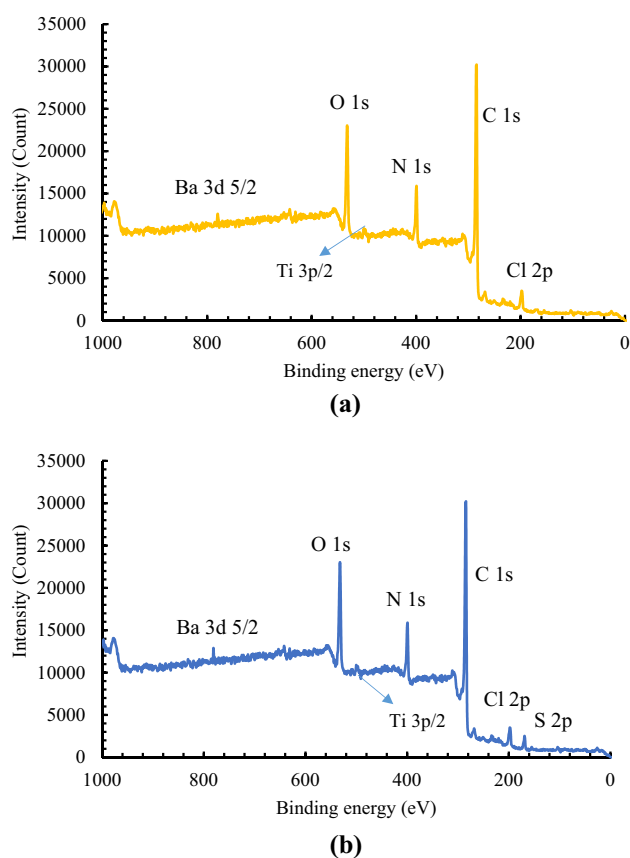


**Fig. 4** XPS of **a** BTO@PANI (1), **b** BTO@PANI (2)

with bending vibrational modes of quinonic-type rings [33], indicating that PANI was formed. The FT-IR spectrum of BTO@PAN(2) show sharp peaks characterizing for  $\text{BaSO}_4$  at 1187, 1055, and  $980\text{ cm}^{-1}$ , which are related to stretching and bending vibrations for  $\text{S}=\text{O}$ , besides bands at 603, and  $638\text{ cm}^{-1}$  refers to  $\text{O}-\text{S}=\text{O}$  bridge, and  $\text{Ba}-\text{O}$  bond, respectively [34, 35]. The shift in the  $\text{Ti}-\text{O}$  band referring to the presence of interaction between BTO and PANI molecules.

SEM images of PANI, BTO, and BTO@PANI composite samples are shown in Fig. 3. Figure 3.a shows that BTO particles appear as granules with sizes distributed in a range of 500–700 nm. Figures 3b–c demonstrate a flake-like morphological structure for PANI(2) with a size less than that obtained for PANI(1). SEM micrograph of BTO@PANI(1) composite (Fig. 3d) shows a plate-like structure with a size less than that of BTO@PANI(2) composite (Fig. 3e). It can be noticed from the SEM figures that the change in the type

of oxidizer lead to a slight change in the surface morphology of both PANI samples and their composites [36]. Moreover, the micrographs of the composite refer to that the PANI structure covers the granules of BTO which extends the diffusing distance for ingredients from the core [37, 38].

XPS spectra analyzed the surface composition of BTO@PANI composites samples. The results are shown in Fig. 4. It shows that composites contain mainly Ba, S, C, N, Cl, and O elements listed in Table 2.

To examine the thermal stability of the prepared materials, thermogravimetric analysis (TGA) was carried out at a temperature range between 25 and  $600\text{ }^\circ\text{C}$  and a heating rate of  $10\text{ }^\circ\text{C min}^{-1}$ . The results obtained are shown in Fig. 5, which shows that the degradation trend of PANI differs from that found for its composite. The thermal degradation of PANI occurs in several steps, the 1<sup>st</sup> step at a lower temperature (up to  $240\text{ }^\circ\text{C}$ ) is mainly due to the release of either water (up to  $125\text{ }^\circ\text{C}$ ) or the removal of the dopant anions (up to  $240\text{ }^\circ\text{C}$ ). The weight loss occurring at temperatures higher than  $240\text{ }^\circ\text{C}$  is attributed to the decomposition of the polymer [39]. The TGA thermograms of the composites samples show smaller weighing loss values than those of their corresponding polyaniline at the same temperature. This reduction in the weighing loss could be attributed to the presence of some interactions between PANI and BTO Molecules.

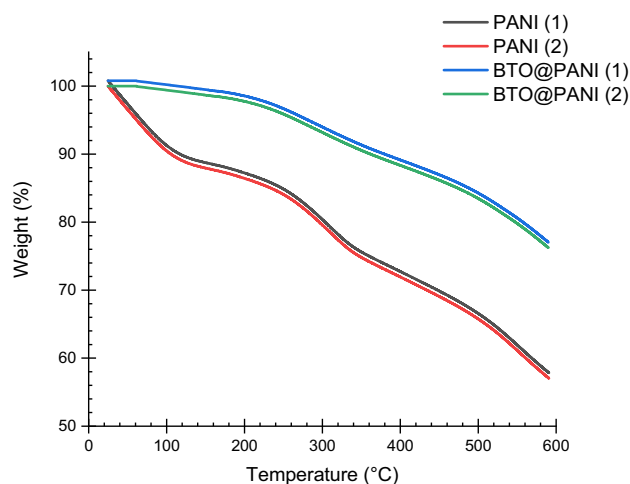


**Fig. 5** TGA of PANI, and BTO@PANI samples

**Table 2** Elemental analysis of BTO composites by XPS technique

Sample	Elements ratio (%)						
	Ba	Ti	S	C	N	O	Cl
BTO@PANI (1)	1.1	0.1	–	86.5	4.9	4	3.4
BTO@PANI (2)	1.2	0.1	0.8	86.6	4.3	4.2	2.8

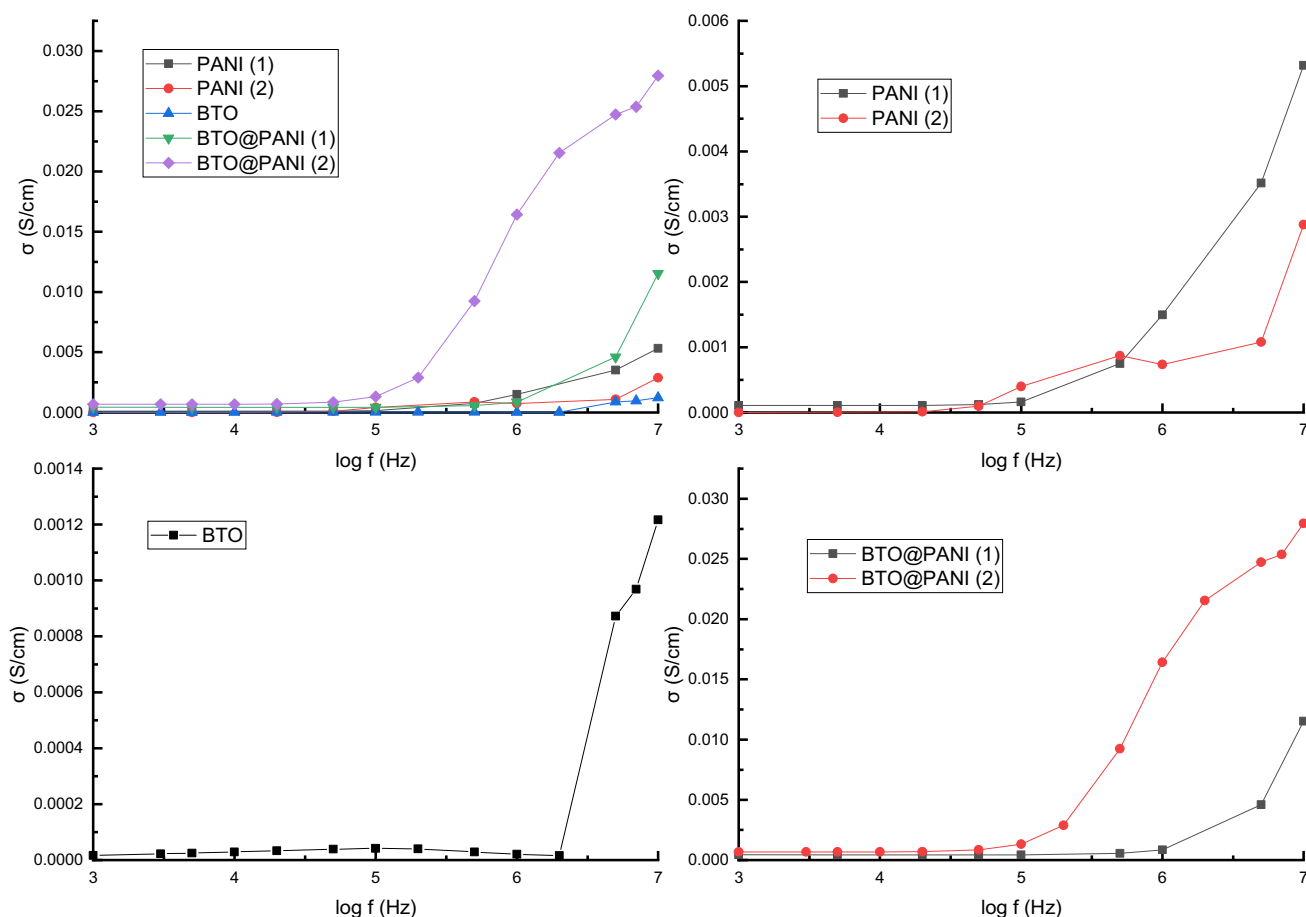


Fig. 6 Effect of frequency on  $\sigma_{AC}$  for the investigated materials

Table 3 Effect of frequency on dielectric data of the prepared materials at room temperature

Sample	1000 Hz			500 kHz			10 MHz			$R_b$ ( $\Omega$ )
	$\sigma$ (S/cm)	$\epsilon'$	$\epsilon''$	$\sigma$ (S/cm)	$\epsilon'$	$\epsilon''$	$\sigma$ (S/cm)	$\epsilon'$	$\epsilon''$	
PANI (1)	$1.1 \times 10^{-4}$	$5 \times 10^5$	$3.0 \times 10^6$	$9.1 \times 10^{-4}$	$4.1 \times 10^1$	$0.94 \times 10^2$	$5.5 \times 10^{-3}$	0.8	0.6	545
PANI (2)	$8.1 \times 10^{-5}$	$3.01 \times 10^6$	$7.1 \times 10^8$	$7.1 \times 10^{-4}$	$4.6 \times 10^1$	$6.2 \times 10^1$	$2 \times 10^{-3}$	13.8	1.1	685
BTO	$1.5 \times 10^{-5}$	$5.53 \times 10^2$	$1.4 \times 10^3$	$5.6 \times 10^{-5}$	2.7	$3.6 \times 10^1$	$9.6 \times 10^{-4}$	1.35	$6 \times 10^{-2}$	$8.7 \times 10^4$
BTO@PANI (1)	$1.0 \times 10^{-3}$	$9.0 \times 10^6$	$1 \times 10^{10}$	$1.2 \times 10^{-3}$	$0.87 \times 10^2$	$0.18 \times 10^2$	$1.1 \times 10^{-2}$	18	7.3	879
BTO@PANI (2)	$6 \times 10^{-4}$	$1.1 \times 10^6$	$9.6 \times 10^7$	$1 \times 10^{-3}$	$1.72 \times 10^2$	$1.52 \times 10^2$	$2.8 \times 10^{-2}$	15.31	4.7	563

### 3.2 Electrical Studies

Electrical properties of pure PANI samples, BTO, and BTO@PANI composites were studied at room temperature, and frequencies ranged between  $10^3$  and  $10^7$  Hz. The ac-conductivity ( $\sigma_{Ac}$ ) of all samples is illustrated in Fig. 6. The conductivity of all samples is almost constant with increasing frequency till  $\sim 5 \times 10^5$  Hz, followed by a sharp increase at higher frequencies owing to universal power law [27]. At all frequencies, the conductivity increases in order: BTO@PANI (2) > BTO@PANI (1) > PANI (1) > PANI (2) > BTO.

The conductivity data obtained are summarized in Table 3. The higher conductivity values of the composite than those of PANI could be interpreted based on the that the electronic charge transfer in the PANI sample, which has a shorter electronic resonance, is going to be less scattered through their transfers in the BTO@PANI composites [40].

The electrical properties of the investigated samples were analyzed using EIS spectroscopy. The results obtained are represented as Cole–Cole diagrams in Fig. 7. The impedance spectra seem to be constituted of overlapping semi-circles without inclined lines at the low-frequency region,

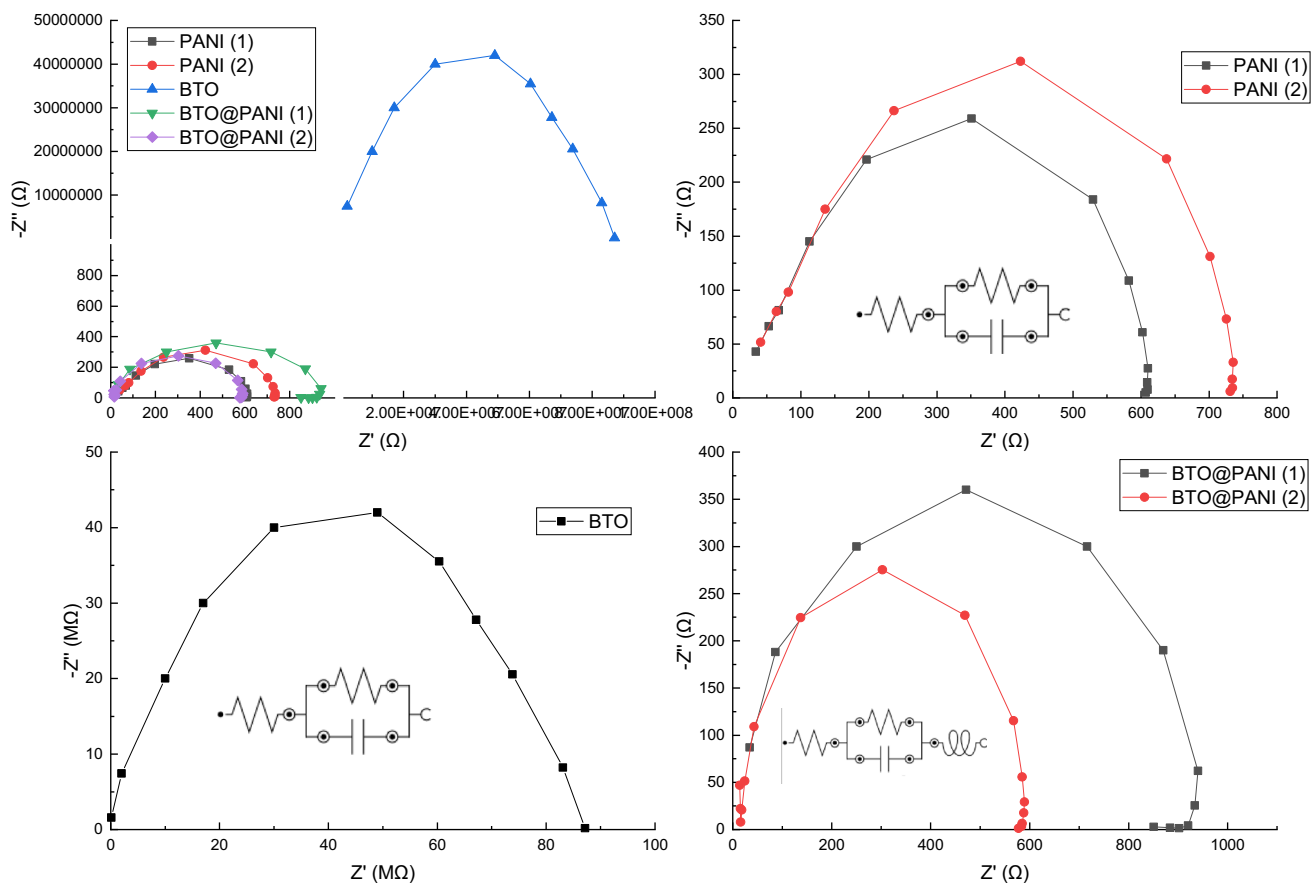


**Fig. 7** Effect of frequency on EI for the investigated materials

indicating the pure electronic conduction process. Each semicircle corresponds to one effect. The semicircles at higher frequencies belong to the grain effect and at low frequencies to the grain boundary. Each semicircle can be represented as a parallel combination of resistance and capacitance for each region. The EIS data obtained for all samples are summarized in Table 3. From which it can be seen that the bulk resistance  $R_b$  increases in the order:

BTO@PANI (1) > BTO@PANI (2) > PANI (2) > PANI (1) > BTO.

The effect of frequency on dielectric constant ( $\epsilon'$ ), and dielectric loss ( $\epsilon''$ ) for

the investigated materials are represented in Fig. 8. For all samples, a dielectric dispersion was observed where both  $\epsilon'$ ,  $\epsilon''$  values reduce fast with raising the frequency in the low-frequency region and approach a nearly frequency-independent trend at higher frequencies. This can be explained based on the decrease in the dipoles polarization when the electric field spreads at higher frequencies [41]. It can also be said that, in nanostructured dielectric materials, interfaces with considerable volume fractions hold a huge number of defects, such as vacancies, dangling bonds, and micro porosities. These defects can alter positive and negative space

charge distribution at interfaces [40]. Upon applying the electric field, the space charges transfer, and when defects catch them, many dipole moments are created. At lower frequencies, these dipole moments are simple to track the variation in the electric field. Consequently, the dielectric loss and the dielectric constant exhibit a large value at low frequency, as listed in Table 3.

### 3.3 Electrochemical Measurements

Cyclic voltammograms for the investigated materials measured in 1 M LiNO<sub>3</sub> aqueous solution at a scan rate of 5 mV/s are shown in Fig. 9. The CV plot of the BTO sample shows a pseudocapacitive behavior with a pair of redox peaks at -0.08 V and +0.24 V, which refers to the Ti<sup>4+</sup> ↔ Ti<sup>3+</sup> process [25]. CV voltammogram of PANI (1) showed a couple of redox peaks at -0.77 V and -0.45 V due to LES ↔ ES ↔ PRG transformations, respectively [42]. Moreover, other reduction peaks also appeared at -0.52 V and -0.65 V, referring to PRG ↔ ES ↔ LES. CV plot of PANI (2) showed a shift in the redox peaks to appear at -0.95 V and -0.052 V due to LES ↔ ES ↔ PRG transformations, respectively [42]. Moreover, a shift and reduction



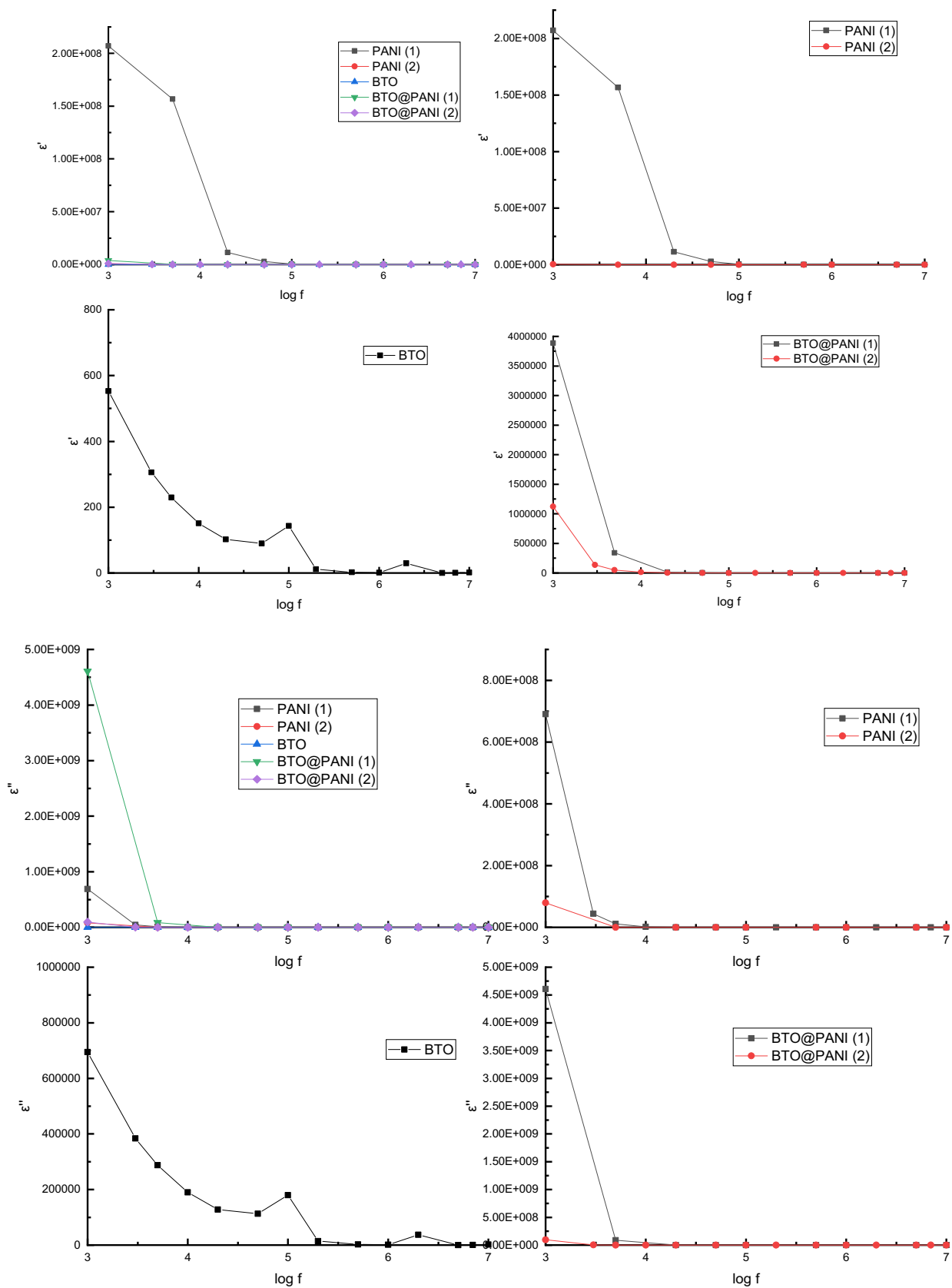
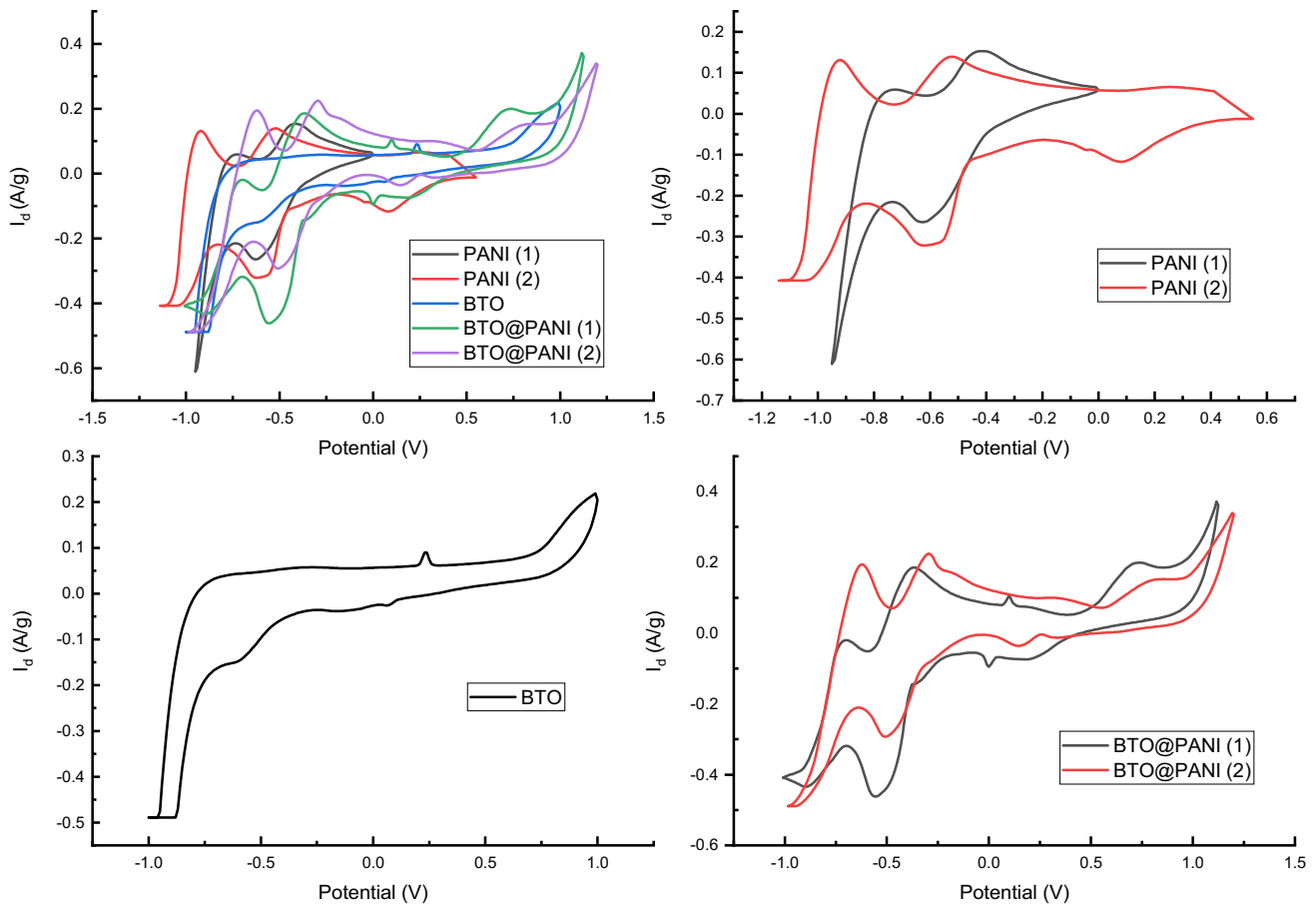


Fig. 8 Effect of frequency on  $\epsilon'$ ,  $\epsilon''$  for the investigated materials



**Fig. 9** CV of the investigated materials

**Table 4** Electrochemical capacitive data of the investigated materials

Sample	$C_{sp}$ (F/g)	$C'$ (F)	$C''$ (F)	$W_D$ ( $\Omega$ )	$\tau$ (s)	$R_s$ ( $\Omega$ )	$R_{ct}$ ( $\Omega$ )
BTO	30	$4.9 \times 10^{-6}$	$8.2 \times 10^{-6}$	108	$7 \times 10^{-4}$	20	120
PANI (1)	49	$4 \times 10^{-7}$	$5 \times 10^{-6}$	79	$3 \times 10^{-4}$	23	45
PANI (2)	42	$4.5 \times 10^{-7}$	$5.3 \times 10^{-6}$	88	$3.6 \times 10^{-4}$	40	51
BTO @PANI (1)	70	$1.2 \times 10^{-5}$	$4.1 \times 10^{-5}$	53	$1.6 \times 10^{-3}$	15	42
BTO @PANI (2)	76	$1.6 \times 10^{-5}$	$4.5 \times 10^{-5}$	55	$1.8 \times 10^{-3}$	38	20

in the peaks' intensities appeared at  $-0.55$  V and  $0.09$  V, referring to  $PRG \leftrightarrow ES \leftrightarrow LES$ . The specific capacity ( $C_{sp}$ ) for each investigated sample was calculated from CV data according to Eq. (5) [43, 44], and the results obtained are listed in Table 4

$$C_{sp} = \frac{1}{m\nu\Delta V} \int_{-V}^{+V} IVdV \quad (5)$$

where  $I$  is current (A),  $V$  is applied potential (V),  $\nu$  is scan rate (V/s), and  $m$  is mass of active material (g).

The CV plots of BTO@PANI composite samples, Fig. 9, show the redox peaks characterized for each of their constituents with a slight shift ranging at  $\pm 0.02$  V, owing to interaction occurring between BTO and PANI.

As shown in Fig. 9, and results in Table 4, the change of oxidizer in PANI formation leads to a slight change in PANI electrochemical behavior. However, it keeps the same electrochemical redox processes of polymer. The particle size of the composite materials is smaller than that of its constituents. Therefore, it is expected that the composites have a higher surface area and more active sites for faradic reaction [45], and larger specific capacitance than pure PANI and BTO. The improvement of the capacitance for the BTO@

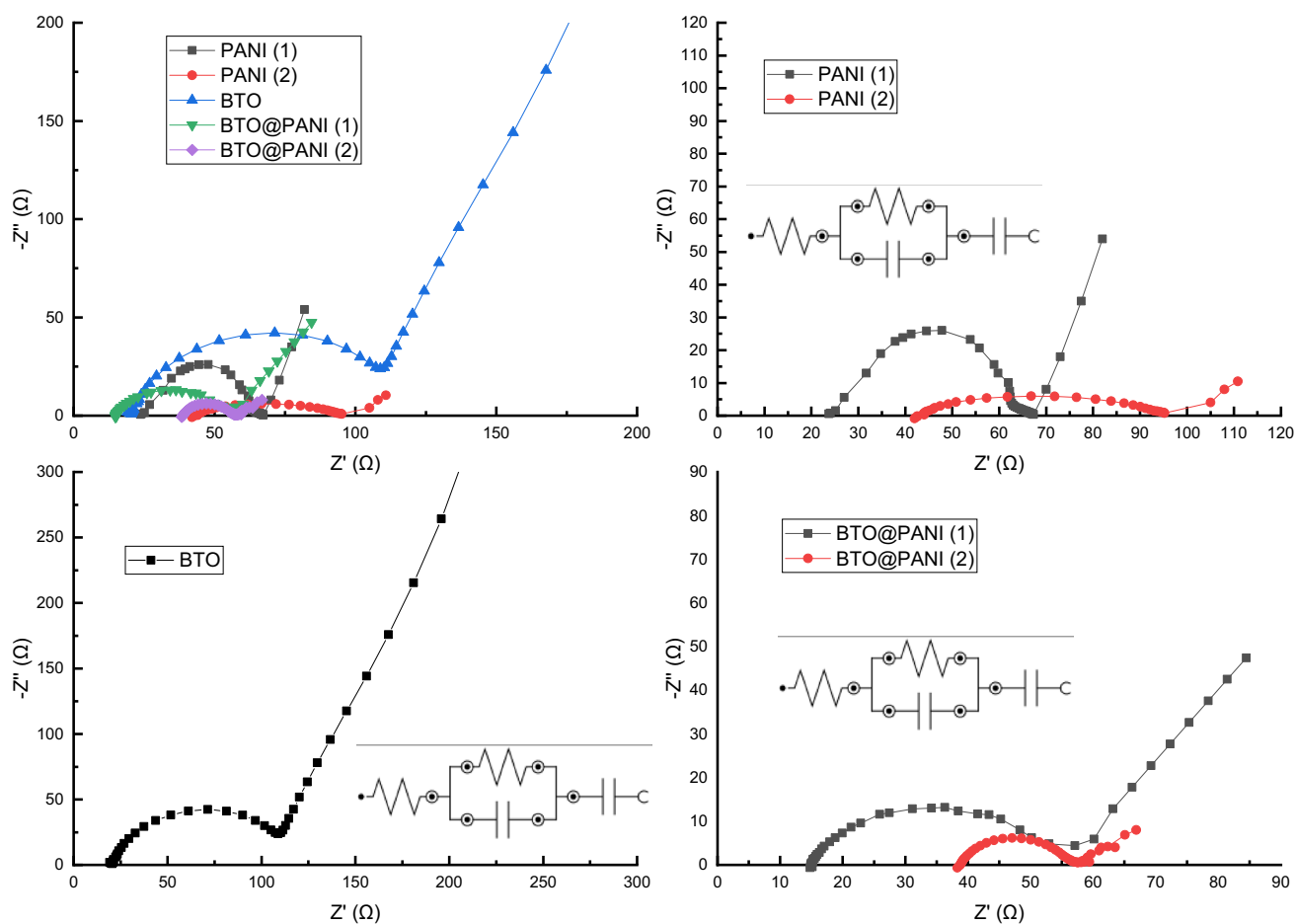


**Fig. 10** EIS of the investigated materials

PANI composites may be also due to the high conductivity of the composites compared with their constituents. All of these refer to that the composite exhibits a more efficient matrix for charge transport, which may provide a large surface area allowing better electrolyte access and storing the charges [46].

Electrochemical impedance spectroscopy (EIS) measurement was performed to understand charge transfer kinetics. The Nyquist plots of investigated electrodes over a  $10^{-2}$ – $0^5$  Hz frequency range are given in Fig. 10. All the samples showed almost the same behavior for each plot, a semicircle in the high-frequency region and a Warburg line in the low-frequency region. In the high-frequency region, the intercept of the semicircle on the  $z^{\prime}$ -axis represents ESR which specifies the ohmic resistance of the electrolyte, the interfacial contact resistance between current collectors and active materials, and the intrinsic resistance of active materials [17]. The semicircle diameter represents the sum of the electrolyte resistance ( $R_s$ ) and the charge transfer resistance ( $R_{ct}$ ) at the electrode/electrolyte interface [47]. These results indicate that the high-frequency semicircle can be attributed

to the charging and discharging process inside the material that corresponds to the charge transfer resistance ( $R_{ct}$ ) of the electrodes and electrolyte interface [45, 46, 48]. The acquired impedance data are listed in Table 4, which show that  $R_{ct}$  increases in the order of.

$BTO > PANI(2) > PANI(1) (> BTO@PANI(1) > BTO@PANI(2))$ . The decrease in the charge-transfer resistance of the composites compared with their constituents reveals that introducing PANI into BTO material causes an increase in Li-ion conductivity in the electrode–electrolyte interface, which results in facilitating the transfer of the charge through phase limit [46, 49].

The spike observed on the Nyquist plot for each electrode at the low-frequency section points to the distinctive character of supercapacitors. The spike stands for the electrode's Warburg impedance ( $W_D$ ), i.e., the diffusive resistance of  $Li^+$  and  $NO_3^-$  ions into the electrode [45].

The electrochemical parameters of the investigated supercapacitor devices were also determined from EIS data using the following Eqs. (6–9) [50]

$$C' = \frac{Z''}{\omega(z)^2} \quad (6)$$

$$C'' = \frac{Z'}{\omega(z)^2} \quad (7)$$

$$\omega = \frac{1}{R.C} \quad (8)$$

$$\omega \tau = 1 \quad (9)$$

The real part  $C'$  is defined as the effective capacitance that the device can deliver, and the imaginary part  $C''$  is related to the irreversible resistivity loss in the device. The frequency  $f$  is the character frequency at which  $C$  reaches the maximum, and  $\tau = 1/f$  is the time constant of the device, which is characteristic of the rate capability. The evaluated electrochemical parameters are listed in Table 4.

## 4 Conclusion

This work aimed to investigate the effect of the synthetic conditions on the electrical and electrochemical properties of PANI and PANI@BTO nanocomposites. First, PANI was synthesized by the polymerization of an aniline monomer via in situ polymerization method using two different oxidizers of dichromate (PANI (1)) and persulphate (PANI (2)). The products were blended with BaTiO<sub>3</sub> (BTO) to form BTO@PANI composites. The synthesized materials were analyzed by FTIR, XRD, XPS, SEM, and TGA. The XPS results confirm the existence of polymer and BTO in nanocomposites. XRD and FTIR results demonstrated the presence of some interactions between BTO and PANI in the PANI-BTO nanocomposite. SEM images showed the polymerization dispersion of Polyaniline on the BTO surface. TGA studies revealed that the thermal stability of the PANI polymers is enhanced in the nanocomposites. Changing the type of oxidizer through the polymerization process of PANI led to a significant change in the electrical conductivity, dielectric and supercapacitive properties of all the investigated samples. The PANI-BTO nanocomposite exhibit remarkable improvement in electrical conductivity, dielectric properties, and enhanced electrochemical performance of the composite in the following order: BTO > PANI(1) > PANI(2) > BTO@PANI(1) > BTO@PANI(2). This enhancement may result from the synergistic effect between PANI and BTO and the decrease of the charge transfer resistance. Due to the low cost and high electrical and electrochemical properties of

PANI-BTO composites, they can be used for several economic biological, and electronic applications like sensors, biosensors, energy storage devices, and electronic circuits.

**Author Contributions** M. A. M primarily designed the study and supervised the experimental research and took the responsibility of explanation of electrochemical studies. K. F. Q performed the preparation of the materials for the whole series of measurements and carried out the explanation of characterizations. All authors discussed the results and commented on the manuscript.

**Funding** Open access funding provided by The Science, Technology & Innovation Funding Authority (STDF) in cooperation with The Egyptian Knowledge Bank (EKB).

**Data Availability** The data that support the findings of this study are available from the corresponding author upon reasonable request.

## Declarations

**Conflict of interest** The authors declare no competing interests.

**Consent for Publication** I declare that this paper consists of original, unpublished work which is not under consideration for publication elsewhere and that all co-authors have approved the contents of this manuscript and submission.

**Research Involving Human and Animal Participants** This article does not contain any studies with human participants or animals performed by any of the authors.

**Open Access** This article is licensed under a Creative Commons Attribution 4.0 International License, which permits use, sharing, adaptation, distribution and reproduction in any medium or format, as long as you give appropriate credit to the original author(s) and the source, provide a link to the Creative Commons licence, and indicate if changes were made. The images or other third party material in this article are included in the article's Creative Commons licence, unless indicated otherwise in a credit line to the material. If material is not included in the article's Creative Commons licence and your intended use is not permitted by statutory regulation or exceeds the permitted use, you will need to obtain permission directly from the copyright holder. To view a copy of this licence, visit <http://creativecommons.org/licenses/by/4.0/>.

## References

1. D. Corzo, G. Tostado-Blázquez, D. Baran, *Front. Electron.* **1**, 1 (2020)
2. N. Phatharapeetranun, V. Esposito, B. Ksapabutr, D. Marani, J.R.J. Bowen, *Mater. Chem. C* **5**, 12430–12440 (2017)
3. K. Namsheer, C.S. Rout, *RSC Adv.* **11**, 5659 (2021)
4. Zhou, T.; Engineering, B.; Beijing, T.; Beijing, T. 19th Int. Conf. Compos. Mater. 1 (2012)
5. H. Ding, M. Zhong, Y.J. Kim, P. Pholpabu, A. Balasubramanian, C.M. Hui, H. He, H. Yang, K. Matyjaszewski, C.J. Bettinger, *ACS Nano* **8**, 4348 (2014)
6. R.K.L. Tan, S.P. Reeves, N. Hashemi, D.G. Thomas, E. Kavak, R. Montazami, N.N.J. Hashemi, *Mater. Chem. A* **5**, 17777 (2017)
7. S. Padmajan Sasikala, K.E. Lee, J. Lim, H.J. Lee, S.H. Koo, I.H. Kim, H.J. Jung, S. Kim, *ACS Nano* **11**, 9424 (2017)

8. T. Nezakati, A. Seifalian, A. Tan, A.M. Seifalian, *Chem. Rev.* **118**, 6766 (2018)
9. Y. Zhang, L. Zhang, K. Cui, S. Ge, X. Cheng, M. Yan, J. Yu, H. Liu, *Adv. Mater.* **30**, 1 (2018)
10. H. Anno, K. Yamaguchi, T. Nakabayashi, H. Kurokawa, F. Akagi, M. Hojo, N.T.I.O.P. Conf, Ser. Mater. Sci. Eng. **18**, 1 (2011)
11. J. Hongxia, L. Qiaoling, Y. Yun, G. Zhiwu, Y. Xiaofeng, *J. Magn. Magn. Mater.* **332**, 10 (2013)
12. L. Yu, Y. Zhu, C. Qian, Q. Fu, Y. Zhao, Y. Fu, *J. Nanomater.* **2016**, 76 (2016)
13. W. Li, F. Gao, X. Wang, N. Zhang, M. Ma, *Angew. Chemie - Int. Ed.* **55**, 9196 (2016)
14. L. Pan, G. Yu, D. Zhai, H.R. Lee, W. Zhao, N. Liu, H. Wang, B.C.-K. Tee, Y. Shi, Y. Cui, Z. Bao, *Proc. Natl. Acad. Sci.* **109**, 9287 (2012)
15. R. Bolagam, R. Boddula, P. Srinivasan, *J. Appl. Electrochem.* **45**, 51 (2015)
16. H. Guo, W. He, Y. Lu, X. Zhang, *Carbon N. Y.* **92**, 133 (2015)
17. Q. Meng, K. Cai, Y. Chen, L. Chen, *Nano Energy* **36**, 268 (2017)
18. K.F. Qasim, W.A. Bayoumy, M.A. Mousa, *J. Mater. Sci. Mater. Electron.* **31**, 19526 (2020)
19. M. Turemis, D. Zappi, M.T. Giardi, G. Basile, A. Ramanaviciene, A. Kapralovs, A. Ramanavicius, R. Viter, *Talanta* **211**, 120658 (2020)
20. N. German, A. Popov, A. Ramanaviciene, A. Ramanavicius, *J. Electrochem. Soc.* **167**, 165501 (2020)
21. S. Ramanavicius, A. Ramanavicius, *Nanomaterials* **11**, 1 (2021)
22. N. German, A. Ramanaviciene, A. Ramanavicius, *Polymers (Basel)*. **12**, 1 (2020)
23. S. Ramanavicius, A. Ramanavicius, *Polymers (Basel)*. **13**, 1 (2021)
24. Z. Durmus, A. Baykal, H. Kavas, H. Szeri, *Phys. B Condens. Matter* **406**, 1114 (2011)
25. M. Khairy, W.A. Bayoumy, K. Faisal, E.E. Elshereafy, M.A. Mousa, *J. Inorg. Organomet. Polym. Mater.* **30**, 3158 (2020)
26. I. Salaoru, S. Paul, *Philos. Trans. R. Soc. A* **367**, 4227 (2009)
27. M.A. Mannaa, K.F. Qasim, F.T. Alshorifi, S.M. El-Bahy, R.S. Salama, *ACS Omega* **6**, 30386 (2021)
28. A. Gabal, *M. Int. J. Electrochem. Sci.* **11**, 4526 (2016)
29. K.F. Qasim, M.A. Mousa, *Egypt. J. Pet.* **30**, 9 (2021)
30. P. Gellings, H. Bouwmeester, *The CRC Handbook of Solid State Electrochemistry*, 1st edn. (CRC Press, US, 1997)
31. M. Khairy, W.A. Bayoumy, K.F. Qasim, E. El-Shereafy, M.A. Mousa, *Mater. Sci. Eng. B Solid State Mater. Adv. Technol.* **271**, 115312 (2021)
32. N. Ahmed, M. Ramadan, W.M.A. El, *Int. J. Hydrogen Energy* **43**, 21219 (2018)
33. V.J. Babu, S. Vempati, S. Ramakrishna, *Mater. Sci. Appl.* **4**, 1 (2013)
34. Á.B. Sifontes, E. Cañizales, J. Toro-mendoza, E. Ávila, P. Hernández, B.A. Delgado, G.B. Gutiérrez, Y. Díaz, E. Cruz-barríos, *J. Nanomater.* **2015**, 1 (2015)
35. S. Golczak, A. Kanciurowska, M. Fahlman, K. Langer, J.J. Langer, *Solid State Ionics* **179**, 2234 (2008)
36. L. Xu, X. Zhang, Z. Chu, H. Wang, Y. Li, X. Shen, L. Cai, H. Shi, C. Zhu, J. Pan, D. Pan, *ACS Appl. Nano Mater.* **4**, 14014 (2021)
37. L. Xu, Z. Chu, H. Wang, L. Cai, Z. Tu, H. Liu, C. Zhu, H. Shi, D. Pan, J. Pan, X. Fei, *ACS Appl. Bio Mater.* **2**, 3429 (2019)
38. L. Xu, H. Wang, Z. Chu, L. Cai, H. Shi, C. Zhu, D. Pan, J. Pan, X. Fei, Y. Lei, *ACS Appl. Polym. Mater.* **2**, 741 (2020)
39. A. Mostafaei, A. Zolriasatein, *Prog. Nat. Sci. Mater. Int.* **22**, 273 (2012)
40. A.S. Roy, S.G. Hegde, A. Parveen, *Polym. Adv. Technol.* **25**, 130 (2014)
41. M. Khairy, A.M. Mousa, *Int. J. Mater. Chem.* **2**, 197 (2013)
42. L. Wang, Y. Ye, X. Lu, Z. Wen, Z. Li, H. Hou, Y. Song, *Sci. Rep.* **3**, 1 (2013)
43. M. Ciszewski, A. Mianowski, P. Szatkowski, G. Nawrat, J. Adamek, *Ionics (Kiel)*. **21**, 557 (2014)
44. M. Khairy, K. Faisal, M.A. Mousa, *J. Solid State Electrochem.* **21**, 873 (2017)
45. P. Genys, E. Aksun, A. Tereshchenko, A. Valiūnienė, A. Ramanaviciene, A. Ramanavicius, *Nanomaterials* **9**, 702 (2019)
46. U. Samukaite-Bubniene, A. Valiūnienė, V. Bucinskas, P. Genys, V. Ratautaite, A. Ramanaviciene, E. Aksun, A. Tereshchenko, B. Zeybek, A. Ramanavicius, *Colloids Surfaces A Physicochem. Eng. Asp.* **610**, 125750 (2021)
47. K. Zhang, L.L. Zhang, X.S. Zhao, J. Wu, *Chem. Mater.* **22**, 1392 (2010)
48. A. Ramanavicius, A. Finkelsteinas, H. Cesiulis, A. Ramanaviciene, *Bioelectrochemistry* **79**, 11 (2010)
49. A.B. Puthirath, B. John, C. Gouri, S. Jayalekshmi, *RSC Adv.* **5**, 69220 (2015)
50. M. Zhi, C. Xiang, J. Li, M. Li, N. Wu, *Nanoscale* **5**, 72 (2013)

**Publisher's Note** Springer Nature remains neutral with regard to jurisdictional claims in published maps and institutional affiliations.